Metals **2015**, *5*, 530-546; doi:10.3390/met5020530

OPEN ACCESS

metals

ISSN 2075-4701

www.mdpi.com/journal/metals/

Article

An *in situ* Study of NiTi Powder Sintering Using Neutron Diffraction

Gang Chen [1,2,*], Klaus-Dieter Liss [3,4] and Peng Cao [1,*]

[1] Department of Chemical and Materials Engineering, the University of Auckland, Private Bag 92019, Auckland 1142, New Zealand

[2] State Key Laboratory of Porous Metal Materials, Northwest Institute for Nonferrous Metal Research, Xi'an 710016, Shaanxi, China

[3] Australian Nuclear Science and Technology Organisation, New Illawarra Road, Lucas Heights, NSW 2234, Australia; E-Mail: kdl@ansto.gov.au

[4] Quantum Beam Science Directorate, Japan Atomic Energy Agency, 2-4 Shirakata-Shirane Tokai-mura, Naka-gun, Ibaraki-ken 319-1195, Japan

* Authors to whom correspondence should be addressed; E-Mails: mychgcsu@163.com (G.C.); p.cao@auckland.ac.nz (P.C.); Tel.: +86-29-8623-1095 (G.C.); Fax: +86-29-8626-4926 (G.C.).

Academic Editor: Hugo F. Lopez

Received: 27 February 2015 / Accepted: 27 March 2015 / Published: 3 April 2015

Abstract: This study investigates phase transformation and mechanical properties of porous NiTi alloys using two different powder compacts (*i.e.*, Ni/Ti and Ni/TiH_2) by a conventional press-and-sinter means. The compacted powder mixtures were sintered in vacuum at a final temperature of 1373 K. The phase evolution was performed by *in situ* neutron diffraction upon sintering and cooling. The predominant phase identified in all the produced porous NiTi alloys after being sintered at 1373 K is B2 NiTi phase with the presence of other minor phases. It is found that dehydrogenation of TiH_2 significantly affects the sintering behavior and resultant microstructure. In comparison to the Ni/Ti compact, dehydrogenation occurring in the Ni/TiH_2 compact leads to less densification, yet higher chemical homogenization, after high temperature sintering but not in the case of low temperature sintering. Moreover, there is a direct evidence of the eutectoid decomposition of NiTi at *ca.* 847 and 823 K for Ni/Ti and Ni/TiH_2, respectively, during furnace cooling. The static and cyclic stress-strain behaviors of the porous NiTi alloys made from the Ni/Ti and Ni/TiH_2 compacts were also investigated. As compared with the Ni/Ti sintered samples,

the samplessintered from the Ni/TiH_2 compact exhibited a much higher porosity, a higher close-to-total porosity, a larger pore size and lower tensile and compressive fracture strength.

Keywords: NiTi; powder sintering; dehydrogenation; neutron diffraction

1. Introduction

NiTi alloys have excellent properties including unique shape memory effect (SME), superelasticity, good biocompatibility and great energy absorption, which have been attracting attention from multiple areas such as medical devices, energy absorbers, actuators and mechanical couplings [1,2]. Powder metallurgy (PM) is a simple, energy-saving and widely used route to produce NiTi alloys [3]. Additionally, powder sintering is an effective technique to produce various porous structures, which are beneficial to bone tissue ingrowth and also provide an effective way of reducing stiffness of the implant [4].

Elemental powder sintering to fabricate porous NiTi alloys has been tremendously successful recently [4–10]. Interestingly, TiH_2 powder was frequently used in NiTi powder sintering in previous studies [4,10–17] due to its cleansing effect of dehydrogenation, which lowers oxygen content and potentially promotes chemical homogenization and densification [18,19]. There is no doubt that the use of TiH_2 favors final phase homogenization after high temperature sintering in the previous reports [4,10–17]. However, our most recent results [10,17,20,21] and the report from Robertson and Schaffer [14] disclosed a discouraging densification and a much larger porosity when using TiH_2 powder. As such, the use of such powder cannot guarantee densification promotion in all NiTi studies, although it does show densification in some other alloys, e.g., pure Ti, Ti-6Al-4V, Ti-5Al-2.5Fe and TiAl [19,22–27]. This might be caused by other factors simultaneously affecting the sintering process and thus the densification. These factors include TiH_2 particle size in Refs. [11,12,28,29] and the binders used in the reports [4,16]. Our recent results [17,20,21] also pointed out that it is the dehydrogenation of TiH_2 powder that increased the porosity of sample and then hindered its densification, when compared with that using similar particle size of Ti powder.

The process of TiH_2 dehydrogenation has been studied for many years [17,19,20,25,27,30–36]. However, most of the studies are conducted in either argon or air atmosphere [15,19,32,33,35]. With respect to the atmosphere, the dehydrogenation usually takes place in the temperature range from 523 to 973 K (250 to 700 °C), which possibly causes the concern of TiH_2 oxidation. On the other hand, some studies, e.g., Refs. [31,34], were performed in vacuum, effectively avoiding the oxidation issue. In spite of this, the diffraction instrument used is laboratory low-intensity X-ray diffraction systems [34], which normally require several minutes to one hour to achieve a complete scan for phase analysis and the achieved data is normally semi-accurate. Such “long”-time scanning properly leads to delayed or missing information. These technical limitations can be tackled with high-energy neutron diffraction under vacuum, which is able to penetrate bulk metals, and this type of diffraction has been successfully employed for *in situ* studies for sintering mechanism and reactions [20,36]. The beam intensities allow information from bulk material to be followed on short time scales (less than 60 s), while undergoing an *in situ* heating/cooling cycle to observe phase transformations. Furthermore, due to the strong incoherent

neutron scattering from hydrogen, neutron diffraction can also track the development of hydrogen concentration during dehydrogenation [20].

Since dehydrogenation of TiH_2 involving in the reaction procedure of powder sintering, this reactive process is thought to be more intricate and different from the case of Ni/Ti blend. To the best of our knowledge, no report has elaborated the reactive sintering mechanism using Ni/TiH_2 blend involving dehydrogenation of TiH_2 and the mechanism investigation of TiH_2 decomposition under vacuum. Bearing in mind, it is of great importance to investigate the combination of dehydrogenation of TiH_2 and newly born Ti and Ni sintering hereafter and the comparative study of mechanical properties of as-fabricated NiTi alloys using Ni/Ti and Ni/TiH_2 powder blends. In this study, it is the first time to observe and study the combined phase transformation processes of dehydrogenation of TiH_2 and the subsequent reactions between new-born Ti and Ni particles using *in situ* neutron diffraction under vacuum as a comparison of the Ni/Ti blend. Further, the systematic mechanical comparison was investigated in terms of pore size, porosity, pore shape and pore size distribution. Therefore, this study is an additional and supplemental report to our recent results in Refs. [17,20].

2. Experimental Section

The mean particle size of Ti, TiH_2 and Ni raw powders used in this study was 32.2, 24.6 and 16.4 μm, respectively. Powder mixtures of Ni/Ti and Ni/TiH_2 were gently mixed in a ball mill for 10 h. Both powder mixtures had a nominal composition of 51 at.% Ni and 49 at.% Ti.

After mixing, powder mixtures were pressed into cylindrical discs of 12 mm diameter with three heights (*i.e.*, 4, 10 and 20 mm for microstructural characterization, neutron diffraction measurement and compression test, respectively) and tensile testing bars (15 mm in gauge length and 2 mm in thickness) in a single-action steel die under 250 MPa pressure. Stearic acid lubricant was slightly applied to the compaction die wall. Subsequently, the 4- and 20-mm-thick green compacts and tensile bars were sintered in a vacuum furnace at 3×10^{-3} Pa, while the 10-mm-thick green compacts were sintered in a high temperature vacuum furnace (5×10^{-4} Pa) equipped on the WOMBAT for *in situ* neutron diffraction measurements. The WOMBAT is a high-intensity diffractometer at the Australian Nuclear Science and Technology Organization (ANSTO), which uses monochromatic neutrons and is equipped with a two-dimensional area detector [37]. The basic technical information of WOMBAT is detailed in Refs. [20,36]. The sintering profile with a heating rate of 5 K/min will be shown in Section 3.2. The heating process was designed into two stages where the first stage is for dehydrogenation of TiH_2 powders, while the second one is to perform final sintering at a temperature of 1373 K (1100 °C) for 2 h, followed by furnace cooling.

A free Rietveld program *MAUD* was chosen to analyze the full powder-diffraction pattern using the Rietveld method, which is to obtain quantitative values of the phase fractions throughout the *in situ* experiments [20]. To determine the phase fractions, each 1-D diffraction pattern was subsequently fed into the Rietveld analysis as a function of time. The analysis was began with a well-fitted analysis file in *MAUD*, which was then used for recursive fitting of the following data files. The batch running was repeated several times with different starting values and constraints to start the iterating process until there was a consistently good fitting throughout the entire run.

Open porosity and sintered density were measured by the Archimedes method as specified in the ASTM B962-08 standard. Pore size distribution analysis was conducted using a pore-size distribution analyzer (GaoQ PDSA-20) using the bubble-point method as per the ASTM F316-03 standard [38]. Microstructures of the as-sintered compacts were observed using an environmental scanning electron microscope (ESEM, FEI Quanta 200F, FEI, Houston, TX, USA) equipped with an energy dispersive X-ray spectrometer (EDX, Oxford Instruments, Oxfordshire, UK). Phase constituents were determined using X-ray diffraction (XRD, Bruker D2 Phaser, Bruker, Karlsruhe, Germany). Differential scanning calorimetry (DSC, Netzsch 404 F3, Netzsch, Selb, Germany) was used to determine the various reactions of compacts during sintering with a heating rate of 5 K/min under flowing argon gas.

The tensile properties of the as-sintered NiTi tensile bars were measured on an Instron 3367 universal machine with a cross-head speed of 0.5 mm/min at ambient temperature. The tensile bars were tensioned approaching to its fracture strength. The compressive properties of the 20-mm-thick samples after 1373 K sintering were measured on an MTS 810 universal machine with a load rate of 0.6 kN/s at room temperature. An alignment cage ensured the parallelism of all samples during testing. The ends of compression cylindrical samples (machined into 10.5-mm diameter and 15-mm height) were polished and smoothed using sand papers, and finally the ends were greased before compression tests. Cyclic experiments were performed to study possible deformation and superelasticity. The cylindrical samples were first compressed until a significant deflection of the linear elastic deformation portion on the stress-strain curve was obtained or the stress level approached to its fracture strength. After that they were unloaded to zero stress and the subsequent cycle followed.

3. Results

3.1. Microstructure

Differential scanning calorimetry (DSC) measurements were conducted to investigate the phase evolution for each compact. Figure 1 shows the DSC curves of the Ni/Ti, Ni/TiH_2 and pure TiH_2 compacts after 250 MPa compaction with a heating rate of 5 K/min. According to Figure 1, a broad exothermic peak can be seen at *ca.* 1036 K for the Ni/Ti compact, which is followed by an endothermic peak developing with an onset temperature at 1143 K. With increasing temperature, this is immediately followed by an apparent exothermic peak at around 1240 K. The final peak is an endothermic peak whose temperature is 1417 K. As discussed in Ref. [20], the four peaks correspond to formation of intermetallic phases (e.g., NiTi, Ni_3Ti and $NiTi_2$, *etc.*), eutectic reaction to generate liquid Ti-rich phase, combustion reaction between molten Ti-rich and Ni-rich phases, and another eutectic reaction between NiTi and Ni_3Ti phases, respectively. In contrast, the dehydrogenation of TiH_2 is a thermally endothermic process [39]. Therefore, the first two endothermic peaks for Ni/TiH_2 and TiH_2 compacts correspond to the dehydrogenation, which ranges from ~630 to 920 K. However, the following peaks for the Ni/TiH_2 are less manifest as compared with the Ni/Ti compact. This is due to the fact that the dehydrogenation peaks may overlap with the following reaction peaks [20].

The X-ray diffraction (XRD) results are presented in Figure 2 for both compacts sintered at 1373 K. It can be seen that the main sintered phase is austenitic B2 NiTi in both cases, with the existence of martensitic B19', secondary $NiTi_2$, Ni_3Ti and Ni_4Ti_3. The existence of these phases in the as-sintered

samples is further confirmed in the ESEM micrographs and EDX analysis (Figure 3). It should be noted that the amount of Ni_4Ti_3 phase is too little to be detected by EDX. The needle-like structural phase is determined to be Ni_3Ti in both samples (Figure 3b,d), which is due to the eutectoid reaction of $NiTi \rightarrow NiTi_2 + Ni_3Ti$ during cooling [20]. However, it is interesting to observe that the amount of secondary phases of the Ni/TiH_2 sintered sample is less compared than that of the Ni/Ti sintered based on the XRD (Figure 2) and energy dispersive X-ray (EDX) results (Figure 3). This means that the final chemical homogeneity of the Ni/TiH_2 sintered is higher than that of the Ni/Ti sintered sample.

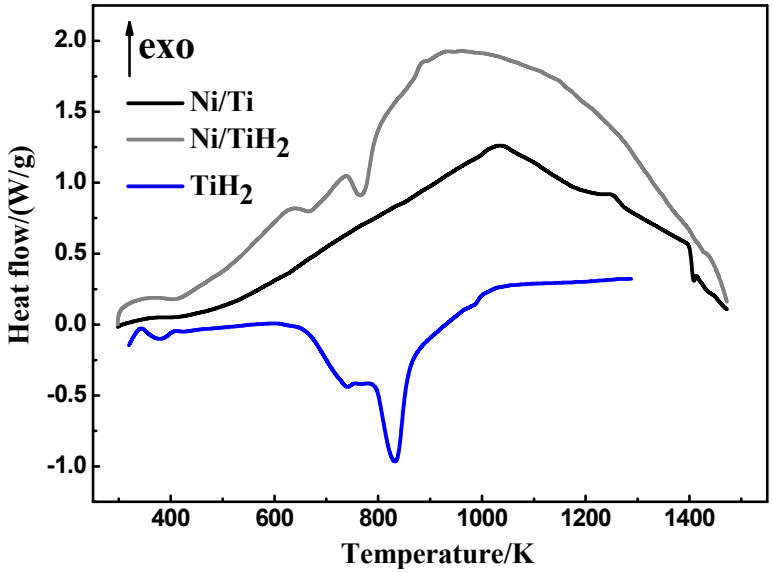

Figure 1. Differential Scanning Calorimetry (DSC) curves of Ni/Ti, Ni/TiH_2 and TiH_2 compacts with a heating rate of 5 K/min.

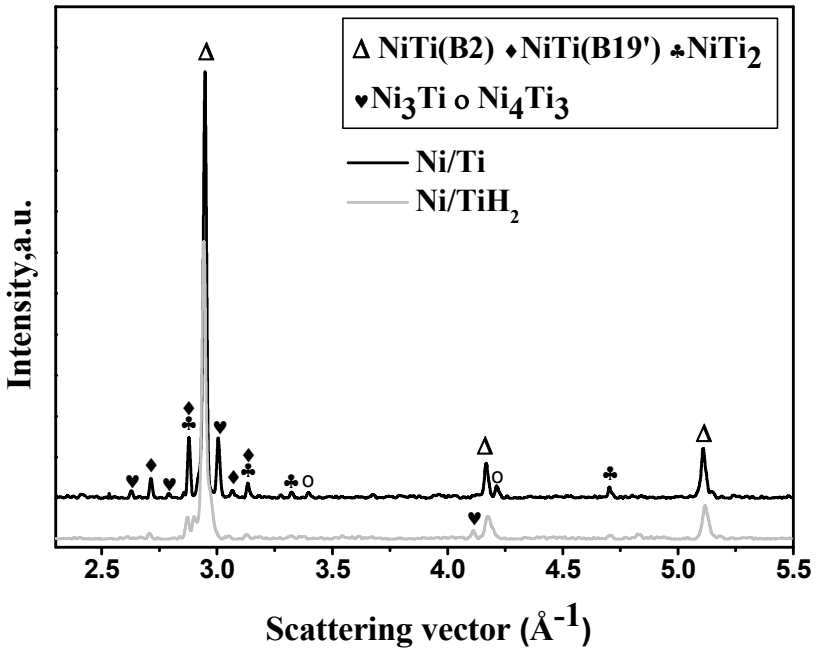

Figure 2. X-ray Diffraction (XRD) patterns of the samples after being sintered at 1373 K.

Table 1 summarizes the basic data of both sintered compacts from 4-mm-thick green samples. It can be figured that the dimension exhibits shrinkage for both sintered samples in terms of either radial or axial direction. Moreover, the shrinkage of the Ni/Ti is larger than that of the Ni/TiH_2 after sintering, with the concomitant higher density for former case. In addition to the shrinkage and density, the open porosity and close-to-total porosity ratio are significantly different from each other. For instance, the close-to-total porosity ratio of the Ni/Ti sintered sample is 89.6% ± 3.4%, while it is only 12.2% ± 0.8% in the case of Ni/TiH_2.

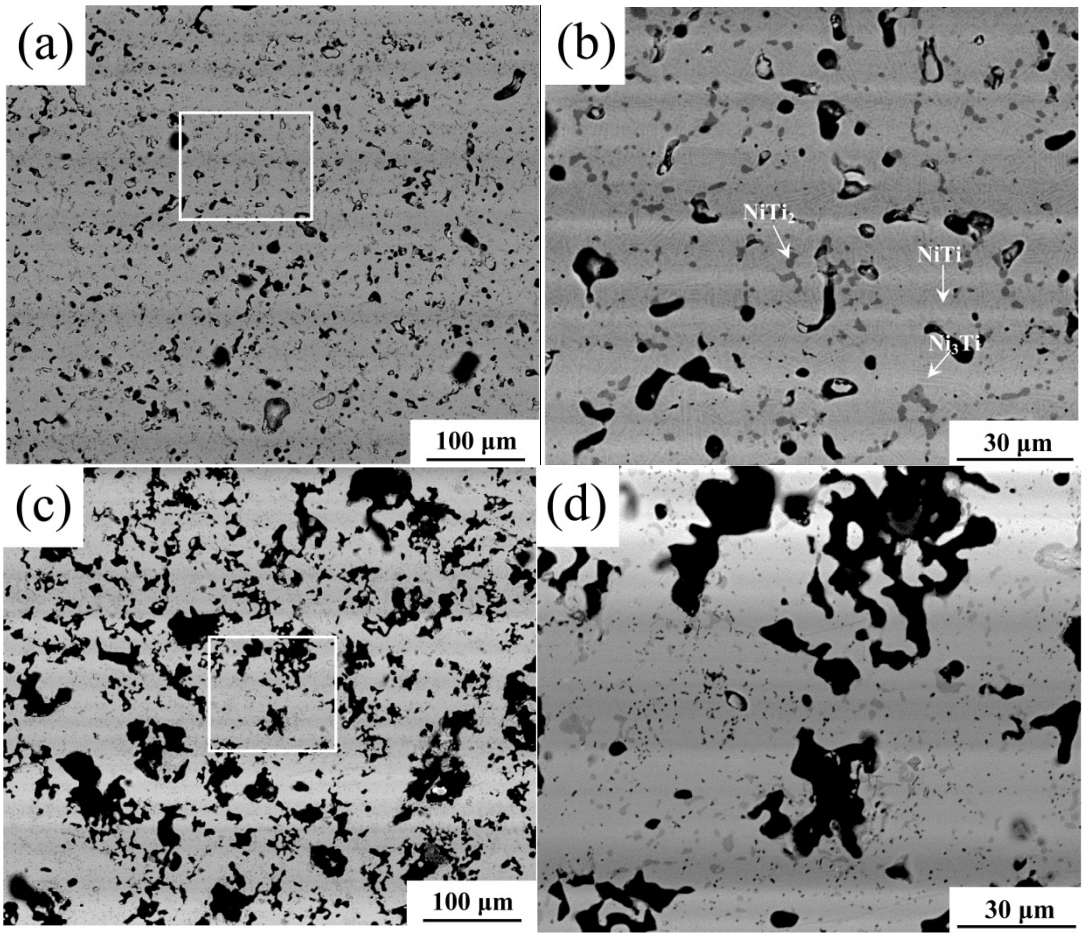

Figure 3. Back-scattered electron images of samples sintered from the Ni/Ti compact at (**a**) 1373 K, (**b**) enlarged square area in (**a**); sintered from the Ni/TiH_2 compact at (**c**) 1373 K, (**d**) enlarged square area in (**c**).

Table 1. Characteristics of the 1373 K sintered porous NiTi samples.

Sample	Shrinkage/%		Density/g·cm^{-3}	Open porosity/%	Close-to-total porosity ratio/%
	axial	radial			
Ni/Ti	10.47 ± 1.23	6.49 ± 0.62	5.81 ± 0.11	1.0 ± 0.1	89.6 ± 3.4
Ni/TiH_2	5.93 ± 0.49	4.21 ± 0.37	4.47 ± 0.07	26.9 ± 2.9	12.2 ± 0.8

3.2. In situ Neutron Diffraction

Figure 4 presents the neutron diffraction patterns of the Ni/Ti and Ni/TiH_2 compacts collected as a function of time in the 2D plot. The intensity is displayed by the grey scale values as a function of

scattering vector Q ($Q = 4\pi/\lambda \cdot \sin\theta$) on the abscissa and time on the ordinate. It is focused on the dehydrogenation process and its effect on the phase transformation of the Ni/TiH_2 compact as compared with the Ni/Ti compact.

From Figure 4a, it can be seen when the temperature approaches *ca.* 840 K, the intensities of intermetallic phases (*i.e.*, B2 NiTi, Ni_3Ti, $NiTi_2$ and Ni_4Ti_3) start to establish as a result of the intensity decrease of elemental Ni and Ti in the Ni/Ti compacts. Afterwards, the intensities of elemental Ni and Ti gradually decrease and it is almost nil at about 1076 K, while these intermetallic phases largely increase. Until the temperature increases to 1163 K, the peaks of some secondary phases (Ni_3Ti and Ni_4Ti_3) almost disappear while the NiTi and $NiTi_2$ phases still remain with temperature increase even when holding at 1373 K. Additionally, it is interesting to note that the intensities of previously disappeared Ni_3Ti and Ni_4Ti_3 phases re-emerge when the furnace was cooled to *ca.* 847 K. This phenomenon has also been discussed in our recent reports [20,36]. It is due to the eutectoid reaction ($NiTi \rightarrow NiTi_2 + Ni_3Ti$) taking place at *ca.* 903 K during furnace cooling [20,36,40–42]. Additionally, it is obvious that the peaks are significantly shifted in position, which is attributed to thermal expansion of crystal lattice when the temperature is relatively high [43]. Moreover, the Mo peaks come from the Mo wires holding the samples in the instrument.

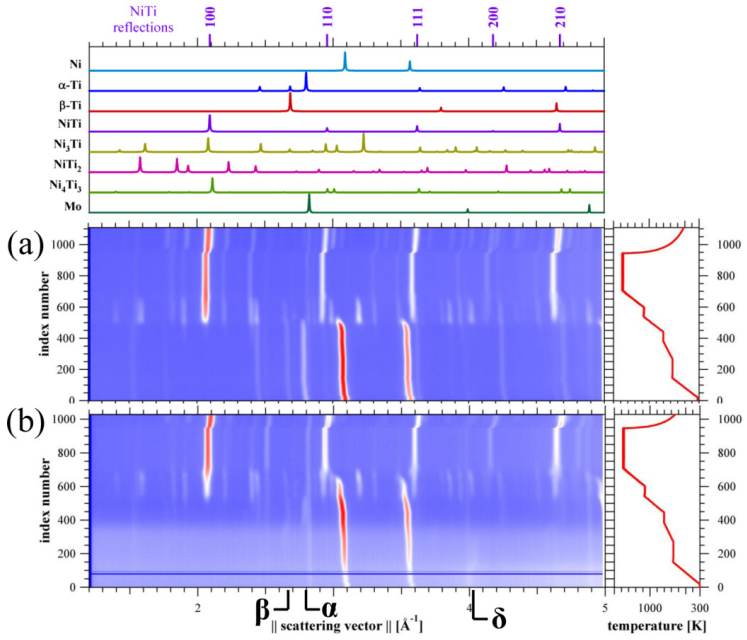

Figure 4. Neutron diffraction patterns as a function of time while temperature is ramped 1373 K from (**a**) Ni/Ti and (**b**) Ni/TiH_2.

In contrast, several differences can be seen between the Ni/TiH_2 compact (Figure 4b) and Ni/Ti compact (Figure 4a) in the heating and cooling process. First, when involving TiH_2 sintering, the initial background is much more significant compared to the Ni/Ti case (Figure 2a). Second, the temperature to establish intensities of intermetallic phases (*i.e.*, B2 NiTi, $NiTi_2$ and Ni_3Ti) is nearly 100 K higher than the Ni/Ti (Figure 4b *cf.* Figure 4a). Third, there is no Ni_4Ti_3 phase formed during sintering in the Ni/TiH_2 case and the intensities of secondary phases are weaker as compared to the Ni/Ti sample. The initial pattern background is caused by the strong incoherent neutron scattering from hydrogen atoms in TiH_2. Then, it gradually decreases with the temperature till ~923 K when it is thought the dehydrogenation of

δ-Ti(H) is almost complete. It is noteworthy that both α-Ti(H) and β-Ti(H) phases appeared during decomposition of TiH_2 below 780 K, which is consistent with the recent study by Jiménez *et al.* [33]. Several intermetallic phases (*i.e.*, B2 NiTi, Ni_3Ti and $NiTi_2$) start to form when the temperature reaches ~975 K concomitant with the intensity decrease of elemental Ni and Ti. After this, the intensities of these phases continue to increase until the temperature rises to ~1350 K when the peaks of Ni, Ti and Ni_3Ti phases disappear. There only exist B2 NiTi and minor $NiTi_2$ phases when holding at 1373 K. It is similar with the case of Ni/Ti compact that the intensity of Ni_3Ti phase starts to re-establish when it was cooled to ~823 K.

With a particular focus on the dehydrogenation process of TiH_2, it can be seen from Figure 4b that the starting constituent includes δ-Ti(H) phase, and with increasing temperature another two hydrogen-containing solid solutions, *i.e.*, α-Ti(H) and β-Ti(H) phases, establish their intensities. The α-Ti(H) and β-Ti(H) phase has hcp and bcc structure, respectively, and hydrogen atoms sit randomly on the tetrahedral sites of both phases [44]. When the temperature approaches *ca.* 695 K, the intensity of δ-Ti(H) phase completely vanishes. Afterwards, the β-Ti(H) and α-Ti(H) phases totally transfer to α-Ti phase at ~780 K.

3.3. Pore-Size Distribution

The use of bubble-point method is to measure the pore-size distribution of both green and sintered samples, which can determine the pore-throat size in the pore tunnel as specified in the American Society of Testing Materials (ASTM) F316-03 standard. As presented in Figure 5a, most pores of the green Ni/Ti compact are in the range of 2.5~7.5 μm accounting for about 80% and only few pores are larger than 15.0 μm or smaller than 2.0 μm. In contrast, the original pore size in the green Ni/TiH_2 compact (Figure 5b), which mostly positions less than 5.0 μm, is smaller compared to the green Ni/Ti compact. However, after 1373 K sintering the pore size can be split into two main ranges for each sample, which are 2.5~20.0 and 4.0~20.0 μm for the Ni/Ti and Ni/TiH_2, respectively. This means pore-size distribution is broader and pores become larger after sintering. Such phenomenon is significantly obvious in the Ni/TiH_2 case that pores are previously positioned below 5.0 μm as shown in Figure 5b, while most of them enlarge to the range between 5 and 10 μm, accounting *ca*. 50% porosity, after sintering.

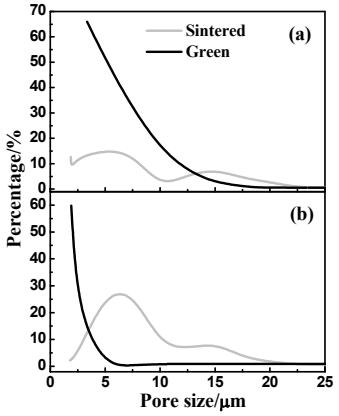

Figure 5. Pore-size distribution of green and 1373 K sintered samples from (**a**) Ni/Ti and (**b**) Ni/TiH_2.

3.4. Mechanical Properties

3.4.1. Static Tensile Test

Figure 6 displays typical stress-strain curves of the NiTi bars being sintered at 1373 K from both compacts. However, both sintered samples exhibited typical brittle fracture behaviors. As presented in Table 2, the fracture tensile strength of the Ni/Ti sintered sample (549.4 ± 9.6 MPa) is much higher than that of the Ni/TiH_2 (160.2 ± 7.3 MPa). Accordingly, the fracture strain of the former sample (4.6% ± 0.2%), which is expectable for porous NiTi, is much higher compared to the later sample (0.9% ± 0.1%). Nevertheless, both Ni/Ti sintered bars demonstrated quasi-linear elastic deformation behavior. In contrast, the Young's modulus of both samples is quite similar but significantly lower than that of the wrought NiTi alloys (~70 GPa) [45].

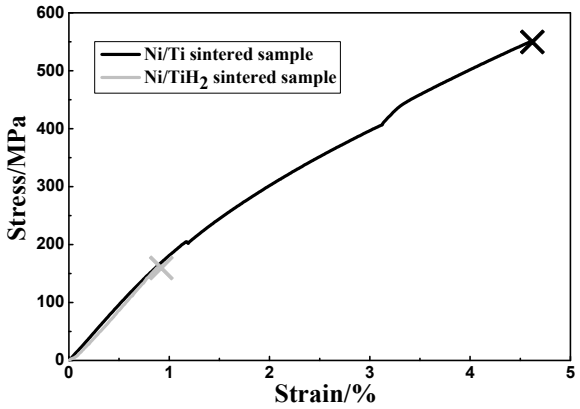

Figure 6. Tensile stress-strain curves for the 1373 K sintered NiTi parts made from Ni/Ti and Ni/TiH_2.

Table 2. Static tensile properties of the as-sintered NiTi alloys.

Sample	Fracture tensile strength/MPa	Fracture strain/%	Young's modulus/GPa
Ni/Ti	549.4 ± 9.6	4.6 ± 0.2	18.9 ± 1.1
Ni/TiH_2	160.2 ± 7.3	0.9 ± 0.1	18.0 ± 0.9

3.4.2. Cyclic Compressive Test

To investigate the porosity effect on the compressive properties, a total of five cycles was applied to each sintered sample. The cyclic compressive samples were compressed to 500, 800 and 1200 MPa, respectively, for the 1373 K-sintered samples from the Ni/Ti compact and then completely unloaded. In the Ni/TiH_2 case, the compressive load changes to 300, 500 and 800 MPa, respectively, since the tensile strength of the Ni/TiH_2 sintered sample is much lower than the Ni/Ti sintered sample (Figure 6). Figure 7 shows the strain curves as a function of time for the compressive cycles. The Ni/TiH_2 sintered sample failed during the third cycle with a fracture strain of 7.14% under 800 MPa stress (Figure 7b). By contrast, the Ni/Ti sintered sample could withstand all the five cycles under both 500 and 800 stresses only, except the 1200 MPa load, where the sample collapsed at the third cycle (Figure 7a).

There can be seen several interesting aspects of superelasticity originating from these curves. First, the residual strain increases with the compressive stress. On the other hand, it is noteworthy that the residual strain of the Ni/Ti sintered sample is less compared with the case of Ni/TiH_2 under the identical compressive load. For instance, the residual strain is 0.75% for the Ni/Ti sintered sample while it is 1.96% in the latter case. Additionally, the maximum strain slightly rises with the cycle number obviously for the higher compressive stress.

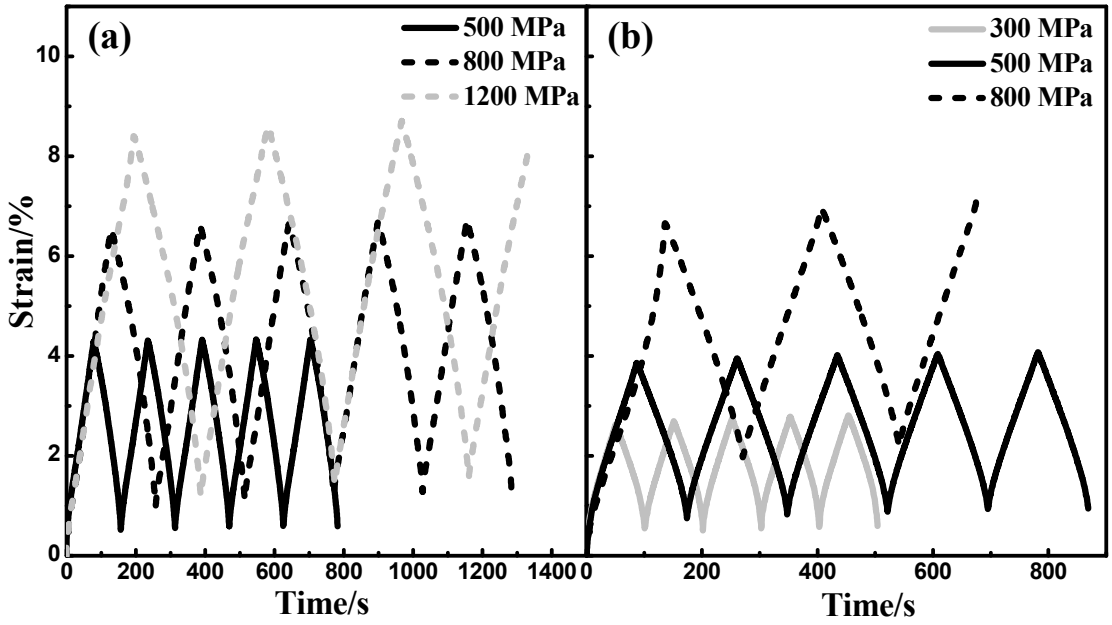

Figure 7. Compressive load-unload-recovery cycles under different compressive stresses for the samples after sintering at 1373 K (**a**) the Ni/Ti compact and (**b**) the Ni/TiH_2 compact. A total of five cycles was applied to each sample.

4. Discussion

4.1. Microstructural Evolution

4.1.1. Dehydrogenation process

Several *in situ*/*ex situ* studies have been focused on the thermal decomposition of TiH_2 [4–35,46,47]. However, it should be noted that the *ex-situ* XRD and TEM investigations may suffer from instant information loss in terms of the phase transformation during the heating process [19,27,30,46,47]. Additionally, although *in situ* high temperature XRD and X-ray synchrotron/neutron diffraction techniques were applied, their results may still be of concern. First, some experiments were conducted in argon atmosphere [32,33,35], which possibly causes the oxidation problem and may mislead the result. Moreover, other reports using vacuum atmosphere may result in instant information loss or delay due to the fact that XRD scanning required a long time (usually several minutes to one hour to achieve a complete scan) [31,34]. To our best knowledge, it is the first time using the neutron diffraction technique to *in situ* investigate the dehydrogenation process of TiH_2. This means could not only solve the long-time scanning problem (needed below 60 s), but also involve vacuum furnace to effectively avoid the oxidation issue.

According to the Ti-H phase diagram (Figure 8), titanium hydride appears as δ, β and α-phase has *ca.* 50~66.7 at.%, 0~50 at.% and 0~8.5 at.% of hydrogen content [48,49], respectively. In our case, the initial titanium hydride phase includes δ phase as shown in Figure 4b. Based on this phase diagram and the neutron diffraction pattern in Figure 4b, it can be concluded that its dehydrogenation could take place as follows: δ → δ + α → δ + β + α → β + α → α. This finding is with great agreement with the report in Ref. [33]. Attributed to the strong incoherent neutron scattering from hydrogen atoms, there is an obvious background during the initial heating. In spite of this, the hydrogen release progresses with the temperature and time concomitant with the background slash. The dehydrogenation temperature range in this study occurs between 573 and 1073 K as presented in our DSC curves (Figure 1) and neutron diffraction pattern (Figure 4b), which is consistent with previous studies [15,30,32,33,50]. As a result, the background evolution is consistent with the process of dehydrogenation during heating and finally almost disappears at about 780 K, Figure 4b.

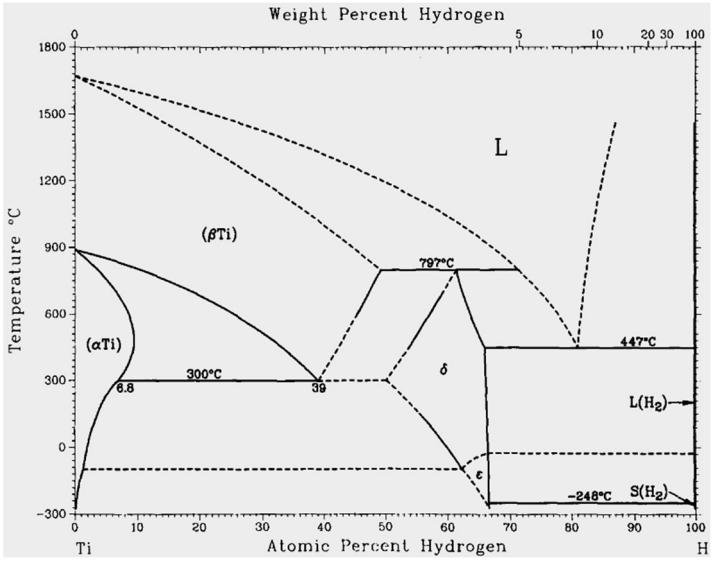

Figure 8. Ti-H binary phase diagram redrawn from Ref. [48].

4.1.2. Pore and Phase Evolution

As discussed in our previous reports [4,10,17,20] together with other studies [5,14,51–56], the pores present in the final sintered samples can be originated from the following four sources: (1) original pores in the green compact, (2) Kirkendall pores formed due to the different diffusion rates between Ni and Ti or newly born Ti elements, (3) pores occurred by the following phase transformation or alloying and (4) large pores caused by liquid phase sintering (LPS). It has been proved in Refs. [17,20] that dehydrogenation in the Ni/TiH_2 compact causes porosity increase during sintering and then the diffusion distance between Ni and new-born Ti particles enlarges, which is thought to delay sequential alloying and increase pore size and porosity in the Ni/TiH_2 sample. In contrast, LPS has two opposite effects on densification. On the one hand, it would favor densification since it promotes diffusion due to the presence of liquid [57,58]. On the other hand, however, it could give rise to swelling because of pores leaving behind [5]. We recall the microstructure images (Figure 3), density and porosity data (Table 1), and pore-size distribution (Figure 5), it seems the combination of the two factors, which are dehydrogenation and LPS, leads to the fact that the density of Ni/Ti sintered sample is much higher

compared to the case of Ni/TiH_2 although the relative density of both green compacts is similar (*i.e.*, it is 73.0% and 71.2% for the Ni/Ti and Ni/TiH_2 compact, respectively).

The Rietveld quantitative analysis from the neutron diffraction data, shown in Figure 9, further supports the discussion above. Figure 9 displays the weight fraction of various intermetallic phases for both compacts during sintering and furnace cooling. It can be confirmed that the whole sintering process of the Ni/TiH_2 compact below 1373 K is postponed compared to the Ni/Ti compact (Figure 9b *cf.* Figure 9a). Nevertheless, at the final holding stage at 1373 K, the amount of B2 NiTi phase is slightly lower for the Ni/TiH_2 compact (94.3 wt.%) than that in the Ni/Ti compact (96.2 wt.%). However, such situation occurs oppositely after furnace cooling, because the final B2 phase amount of the Ni/TiH_2 compact after cooling (87.3 wt.%) is higher as compared to the Ni/Ti compact (81.3 wt.%). This observation has been reported in our recent result [20] that there is a eutectoid reaction NiTi $\rightarrow$ Ni_3Ti + $NiTi_2$ happened at around 903 K, which means the B2 NiTi phase decomposed into Ni_3Ti and $NiTi_2$ phases during cooling and thus gives rise to the phase amount change accordingly. All the amount of secondary phases such as $NiTi_2$, Ni_3Ti and Ni_4Ti_3 in the Ni/Ti sintered sample is higher than that in the Ni/TiH_2 sintered sample, which is consistent with the XRD results (Figure 2). This can further confirm that the dehydrogenation from TiH_2 activates titanium surface and thus enhances final chemical homogenization.

4.2. Fracture, Superelasticity and Modulus

With regard to the strength of a material, it is dependent on the weakest portion in the material. Normally, porosity, pore size and pore shape have a significant effect on the strength of porous NiTi alloys. For instance, a more severe stress concentration may arise from a sharp edge of the pores. Furthermore, a larger pore size and/or higher porosity result in more reduction in the effective load-carrying cross section [10]. These factors all result in the strength drop the porous NiTi alloys [59]. Recalling the fracture tensile strength and Young's modulus (Figures 6 and 7, Table 2), these values of the Ni/Ti sintered sample are higher compared with the Ni/TiH_2 sintered sample.

On the one hand, from a fracture mechanics point of view, the material fails when the stress intensity factor K ($= Y\sigma\sqrt{\pi a}$) reaches its fracture toughness [60]. In this respect, the "a" represents the pore size and pore-size distribution, while the "Y" is a collective parameter of pore shape and orientation in a porous material. In this study, the mean pore size of the Ni/Ti sintered sample is significantly smaller than did in the Ni/TiH_2 case, Figures 3 and 5. However, the ESEM micrographs (Figure 3) show that the pore shape is similar in both samples. This implies that the average "Y" value is analogous in both cases, while the "a" value gives rise to a higher stress intensity factor K for the Ni/TiH_2 sintered sample. As such, the Ni/Ti sintered sample demonstrated a higher fracture stress, as compared to the case of Ni/TiH_2. Alternatively, this means the use of TiH_2 powder leads to lower fracture strength caused by larger pore size and lower densification (Table 1) although it shows higher chemical homogenization (Figure 9).

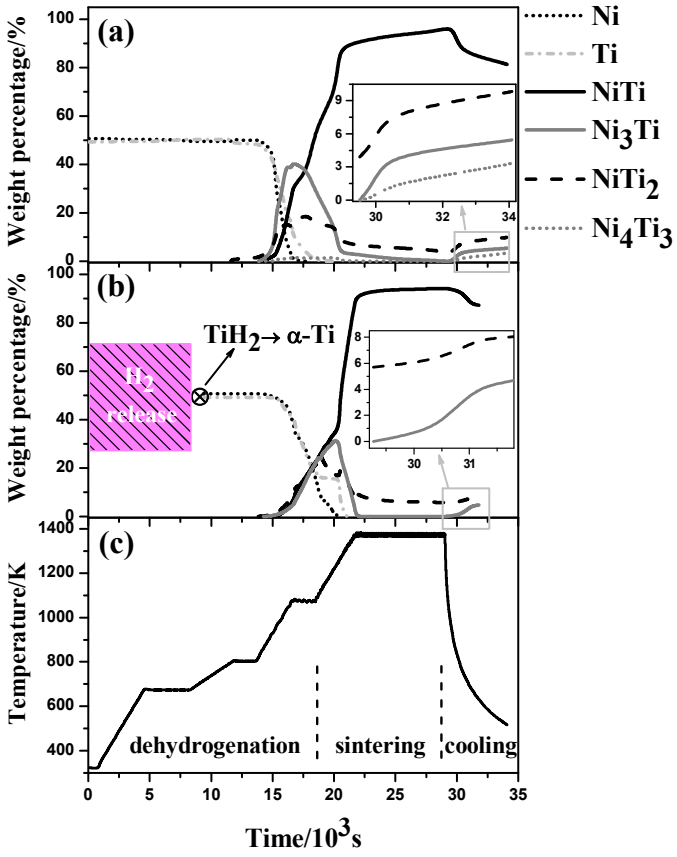

Figure 9. Weight fractions of the detected phases as a function of time (temperature) during *in situ* scan as achieved by Rietveld refinement analysis upon heating and cooling (**a**) the Ni/Ti compact, (**b**) the Ni/TiH_2 compact, and (**c**) heating and cooling profile as a function of time.

On the other hand, compressive tests show the typical superelasticity properties of sintered NiTi alloys, which are attributed to the stress-induced martensitic transformation [2]. With increasing the cycle number, the accumulated residual strain increases and then levels off to a constant value (Figure 7). This phenomenon has been discussed regarding to the general shape memory "training process" [20,61]. The Young's modulus of the Ni/Ti sintered sample is greater than that of the Ni/TiH_2 sintered sample (Table 2). First, as shown in Table 1 the close-to-total porosity ratio is 89.6% ± 3.4% and 12.2% ± 0.8% for the Ni/Ti and Ni/TiH_2 sintered compacts, respectively. Normally, higher ratio of close-to-total porosity would give rise to higher elastic modulus [60,62]. Second, the higher density of the Ni/Ti sintered sample would result in higher elastic modulus than did the Ni/TiH_2 sintered sample after 1373 K sintering as shown in Table 1. Additionally, it should be noted that the final phases present in the sintered compacts also affect the elastic modulus. Recalling Figure 9 that the Ni/TiH_2 sintered compact contains 8.0 wt.% $NiTi_2$ phase while the Ni/Ti sintered sample has 9.8 wt.% $NiTi_2$. More amount of $NiTi_2$ phase also causes higher elastic modulus for the Ni/Ti sintered sample [20].

5. Summary

In this report, porous NiTi alloys from Ni/Ti and Ni/TiH_2 powder compacts were produced by introducing a conventional press-and-sinter method. The microstructure and mechanical properties of sintered samples were investigated and compared with involving the use of TiH_2 powder. The following conclusions can be drawn from this study.

(1) B2 NiTi phase is the dominant phase identified in both samples after being sintered at 1373 K holding for two hours together with the presence of some minor secondary phases.
(2) Dehydrogenation from TiH_2 leads to a lower density, a much higher porosity, a larger pore size but higher final chemical homogenization after sintering as compared with the Ni/Ti compact.
(3) The use of TiH_2 powder causes lower fracture strength and lower elastic modulus compared with the Ni/Ti sintered sample.

Acknowledgments

We acknowledge the financial support from Ministry of Business Innovation and Employment (MBIE), New Zealand. Gang Chen thanks the China Scholarship Council (CSC) for providing him a doctoral scholarship. We also acknowledge the support of the Bragg Institute, Australian Nuclear Science and Technology Organization (ANSTO), in providing the neutron research facilities used in this work. The authors would like to thank Australian Institute of Nuclear Science and Engineering (AINSE) Ltd for providing financial assistance (award No. P2716) to enable work on WOMBAT to be conducted. The authors also appreciate the funding from Shaanxi Science and Technology Co-ordination and Innovation Project (2014KTZB01-02-04).

Conflicts of Interest

The authors declare no conflict of interest.

References

1. Duering, T.W.; Pelton, A.R. *Materials Properties Handbook: Titanium Alloys*; ASM International, the Materials Information Society: Materials Park, OH, USA, 1994.
2. Yamauchi, K.; Ohkata, I.; Tsuchiya, K.; Miyazaki, S. *Shape Memory and Superelastic Alloys: Technologies and Applications*; Woodhead Publishing: Cambridge, UK, 2011; p. 390.
3. Elahinia, M.H.; Hashemi, M.; Tabesh, M.; Bhaduri, S.B. Manufacturing and processing of NiTi implants: A review. *Prog. Mater. Sci.* **2012**, *57*, 911–946.
4. Chen, G.; Cao, P.; Wen, G.; Edmonds, N.; Li, Y. Using an agar-based binder to produce porous NiTi alloys by metal injection moulding. *Intermetallics* **2013**, *37*, 92–99.
5. Whitney, M.; Corbin, S.F.; Gorbet, R.B. Investigation of the mechanisms of reactive sintering and combustion synthesis of NiTi using differential scanning calorimetry and microstructural analysis. *Acta Mater.* **2008**, *56*, 559–570.
6. Sadrnezhaad, S.K.; Hosseini, S.A. Fabrication of porous NiTi-shape memory alloy objects by partially hydrided titanium powder for biomedical applications. *Mater. Des.* **2009**, *30*, 4483–4487.

7. Tosun, G.; Ozler, L.; Kaya, M.; Orhan, N. A study on microstructure and porosity of NiTi alloy implants produced by SHS. *J. Alloys Compd.* **2009**, *487*, 605–611.
8. Whitney, M.; Corbin, S.F.; Gorbet, R.B. Investigation of the influence of Ni powder size on microstructural evolution and the thermal explosion combustion synthesis of NiTi. *Intermetallics* **2009**, *17*, 894–906.
9. Liu, X.; Wu, S.; Yeung, K.W.K.; Xu, Z.S.; Chung, C.Y.; Chu, P. Superelastic porous NiTi with adjustable porosities synthesized by powder metallurgical method. *J. Mater. Eng. Perform.* **2012**, *21*, 2553–2558.
10. Chen, G.; Cao, P.; Edmonds, N. Porous NiTi alloys produced by press-and-sinter from Ni/Ti and Ni/TiH_2 mixtures. *Mater. Sci. Eng. A* **2013**, *582*, 117–125.
11. Li, B.-Y.; Rong, L.-J.; Li, Y.-Y. Stress–strain behavior of porous Ni-Ti shape memory intermetallics synthesized from powder sintering. *Intermetallics* **2000**, *8*, 643–646.
12. Li, B.-Y.; Rong, L.-J.; Li, Y.-Y. The influence of addition of TiH_2 in elemental powder sintering porous Ni-Ti alloys. *Mater. Sci. Eng. A* **2000**, *281*, 169–175.
13. Bertheville, B.; Neudenberger, M.; Bidaux, J.E. Powder sintering and shape-memory behaviour of NiTi compacts synthesized from Ni and TiH_2. *Mater. Sci. Eng. A* **2004**, *384*, 143–150.
14. Robertson, I.M.; Schaffer, G.B. Swelling during sintering of titanium alloys based on titanium hydride powder. *Powder Metall.* **2010**, *53*, 27–33.
15. Wu, S.; Liu, X.; Yeung, K.W.K.; Hu, T.; Xu, Z.; Chung, J.C.Y.; Chu, P.K. Hydrogen release from titanium hydride in foaming of orthopedic NiTi scaffolds. *Acta Biomater.* **2011**, *7*, 1387–1397.
16. Chen, G.; Wen, G.A.; Cao, P.; Edmonds, N.; Li, Y.M. Processing and characterisation of porous NiTi alloy produced by metal injection moulding. *Powder Injection Moulding Int.* **2012**, *6*, 83–88.
17. Chen, G.; Cao, P. NiTi powder sintering from TiH_2 powder: An *in situ* investigation. *Metall. Mater. Trans. A* **2013**, 1–4.
18. Wang, H.; Fang, Z.Z.; Sun, P. A critical review of mechanical properties of powder metallurgy titanium. *Int. J. Powder Metall.* **2010**, *46*, 45–57.
19. Wang, H.T.; Lefler, M.; Fang, Z.Z.; Lei, T.; Fang, S.M.; Zhang, J.M.; Zhao, Q. Titanium and titanium alloy via sintering of TiH_2. *Key Eng. Mater.* **2010**, *436*, 157–163.
20. Chen, G.; Liss, K.-D.; Cao, P. *In situ* observation and neutron diffraction of NiTi powder sintering. *Acta Mater.* **2014**, *67*, 32–44.
21. Chen, G. Powder Metallurgical Titanium Alloys (TiNi and Ti-6Al-4V): Injection Moulding, Press-and-Sinter, and Hot Pressing. Ph.D. Thesis, The University of Auckland, Auckland, New Zealand, 2014.
22. Azevedo, C.R.F.; Rodrigues, D.; Beneduce Neto, F. Ti-Al-V powder metallurgy (PM) via the hydrogenation–dehydrogenation (HDH) process. *J. Alloys Compd.* **2003**, *353*, 217–227.
23. Robertson, I.M.; Schaffer, G.B. Comparison of sintering of titanium and titanium hydride powders. *Powder Metall.* **2010**, *53*, 12–19.
24. Ivasishin, O.M.; Eylon, D.; Bondarchuk, V.I.; Savvakin, D.G. Diffusion during powder metallurgy synthesis of titanium alloys. *Defect Diffus. Forum* **2008**, *277*, 177–185.
25. Zhang, J.M.; Yi, J.H.; Gan, G.Y.; Yan, J.K.; Du, J.H.; Liu, Y.C. Research on dehydrogenation and sintering process of titanium hydride for manufacture titanium and titanium alloy. *Adv. Mater. Res.* **2013**, *616–618*, 1823–1829.

26. Ivasishin, O.M.; Savvakin, D.G.; Froes, F.; Mokson, V.C.; Bondareva, K.A. Synthesis of alloy Ti-6Al-4V with low residual porosity by a powder metallurgy method. *Powder Metall. Metal Ceram.* **2002**, *41*, 382–390.
27. Bhosle, V.; Baburaj, E.G.; Miranova, M.; Salama, K. Dehydrogenation of nanocrystalline TiH_2 and consequent consolidation to form dense Ti. *Metall. Mater. Trans. A* **2003**, *34*, 2793–2799.
28. Li, B.Y.; Rong, L.J.; Li, Y.Y. Porous NiTi alloy prepared from elemental powder sintering. *J. Mater. Res.* **1998**, *13*, 2847–2851.
29. Li, B.-Y.; Rong, L.-J.; Li, Y.-Y.; Gjunter, V.E. An investigation of the synthesis of Ti-50 at. Pct Ni alloys through combustion synthesis and conventional powder sintering. *Metall. Mater. Trans. A* **2000**, *31*, 1867–1871.
30. Bhosle, V.; Baburaj, E.G.; Miranova, M.; Salama, K. Dehydrogenation of TiH_2. *Mater. Sci. Eng. A* **2003**, *356*, 190–199.
31. Sandim, H.R.Z.; Morante, B.V.; Suzuki, P.A. Kinetics of thermal decomposition of titanium hydride powder using *in situ* high-temperature X-ray diffraction (HTXRD). *Mater. Res.* **2005**, *8*, 293–297.
32. Liu, H.; He, P.; Feng, J.C.; Cao, J. Kinetic study on nonisothermal dehydrogenation of TiH_2 powders. *Int. J. Hydrog. Energy* **2009**, *34*, 3018–3025.
33. Jiménez, C.; Garcia-Moreno, F.; Pfretzschner, B.; Klaus, M.; Wollgarten, M.; Zizak, I.; Schumacher, G.; Tovar, M.; Banhart, J. Decomposition of TiH_2 studied *in situ* by synchrotron X-ray and neutron diffraction. *Acta Mater.* **2011**, *59*, 6318–6330.
34. Farhana, H.N.; Wang, Y.; Noor, M.M.; Chan, S.I. Static X-ray scans on the titanium hydride (TiH_2) powder during dehydrogenation. *Adv. Mater. Res.* **2013**, *795*, 124–127.
35. Jiménez, C.; Garcia-Moreno, F.; Pfretzschner, B.; Kamm, P.H.; Neu, T.R.; Klaus, M.; Genzel, C.; Hilger, A.; Manke, I.; Banhart, J. Metal foaming studied *in situ* by energy dispersive X-ray diffraction of synchrotron radiation, X-ray radioscopy, and optical expandometry. *Adv. Eng. Mater.* **2013**, *15*, 141–148.
36. Chen, G.; Liss, K.-D.; Cao, P. *In situ* observation of phase transformation of powder sintering from Ni/TiH_2 using neutron diffraction. In *TMS 2014 Supplemental Proceedings*; John Wiley & Sons, Inc.: Hoboken, NJ, USA, 2014; pp. 967–973.
37. Studer, A.J.; Hagen, M.E.; Noakes, T.J. Wombat: The high-intensity powder diffractometer at the opal reactor. *Phys. B Condens. Matter* **2006**, *385–386*, 1013–1015.
38. Yu, J.; Hu, X.; Huang, Y. A modification of the bubble-point method to determine the pore-mouth size distribution of porous materials. *Sep. Purif. Technol.* **2010**, *70*, 314–319.
39. Viswanathan, B.; Murthy, S.S.; Sastri, M.V.C. *Metal Hydrides: Fundamentals and Applications*, 1st ed.; Springer: Berlin, Germany, 1999; p. 189.
40. Duwez, P.; Taylor, J.L. The structure of intermediate phases in alloys of titanium with iron, cobalt, and nickel. *Trans. AIME* **1950**, *188*, 1173–1176.
41. Poole, D.M.; Hume-Rothery, W. The equilibrium diagram of the system nickel-titanium. *J. Inst. Metals* **1954**, *83*, 473–480.
42. Gupta, S.P.; Mukherjee, K.; Johnson, A.A. Diffusion controlled solid state transformation in the near-equiatomic Ti-Ni alloys. *Mater. Sci. Eng.* **1973**, *11*, 283–297.

43. Liss, K.-D.; Bartels, A.; Schreyer, A.; Clemens, H. High-energy X-rays: A tool for advanced bulk investigations in materials science and physics. *Textures Microstruct.* **2003**, *35*, 219–252.
44. Predel, B. H-Ti (Hydrogen-Titanium). In *Ga-Gd-Hf-Zr*; Madelung, O., Ed.; Springer: Berlin/Heidelberg, Germany, 1996; Volume 5f, pp. 1–2.
45. Greiner, C.; Oppenheimer, S.M.; Dunand, D.C. High strength, low stiffness, porous NiTi with superelastic properties. *Acta Biomater.* **2005**, *1*, 705–716.
46. Mandrino, D.; Paulin, I.; Škapin, S.D. Scanning electron microscopy, X-ray diffraction and thermal analysis study of the TiH_2 foaming agent. *Mater. Charact.* **2012**, *72*, 87–93.
47. Paulin, I.; Donik, Č.; Mandrino, D.; Vončina, M.; Jenko, M. Surface characterization of titanium hydride powder. *Vacuum* **2012**, *86*, 608–613.
48. Okamoto, H. H-Ti (Hydrogen-Titanium). *J. Phase Equilib. Diffus.* **2011**, *32*, 174–175.
49. Fukai, Y. *The Metal-Hydrogen System, Basic Bulk Properties*; 2nd ed.; Springer: Berlin/Heidelberg, Germany, 2005; p. 497.
50. Igharo, M.; Wood, I.V. Compaction and sintering phenomena in titanium-nickel shape memory alloys. *Powder Metall.* **1985**, *28*, 131–139.
51. Biswas, A. Porous NiTi by thermal explosion mode of SHS: Processing, mechanism and generation of single phase microstructure. *Acta Mater.* **2005**, *53*, 1415–1425.
52. Otsuka, K.; Ren, X. Physical metallurgy of Ti-Ni-based shape memory alloys. *Prog. Mater. Sci.* **2005**, *50*, 511–678.
53. Laeng, J.; Xiu, Z.; Xu, X.; Sun, X.; Ru, H.; Liu, Y. Phase formation of Ni–Ti via solid state reaction. *Phys. Scr.* **2007**, *2007*, 250.
54. Bansiddhi, A.; Dunand, D.C. Shape-memory NiTi foams produced by replication of NaCl space-holders. *Acta Biomater.* **2008**, *4*, 1996–2007.
55. Li, H.; Yuan, B.; Gao, Y.; Chung, C.Y.; Zhu, M. High-porosity NiTi superelastic alloys fabricated by low-pressure sintering using titanium hydride as pore-forming agent. *J. Mater. Sci.* **2009**, *44*, 875–881.
56. Wen, C.E.; Xiong, J.Y.; Li, Y.C.; Hodgson, P.D. Porous shape memory alloy scaffolds for biomedical applications: A review. *Phys. Scr.* **2010**, *2010*, 014070.
57. German, R.M. *Powder Metallurgy Science*; Metal Powder Industries Federation: Princeton, NJ, USA, 1998.
58. German, R.; Suri, P.; Park, S. Review: Liquid phase sintering. *J. Mater. Sci.* **2009**, *44*, 1–39.
59. Ashby, M.F.; Evans, A.; Fleck, N.A.; Gibson, L.J.; Hutchinson, J.W.; Wadley, H. *Metal Foams: A Design Guide*; Butterworth-Heinemann: Boston, MA, USA, 2000.
60. Anderson, T.L. *Fracture Mechanics Fundamentals and Applications*, 3rd ed.; CRC Press: Boca Raton, FL, USA, 2005.
61. Nemat-Nasser, S.; Guo, W.-G. Superelastic and cyclic response of NiTi SMA at various strain rates and temperatures. *Mech. Mater.* **2006**, *38*, 463–474.
62. Gibson, L.J.; Ashby, M.F. *Cellular Solids: Structure and Properties*, 2nd ed.; Cambridge University Press: Cambridge, UK, 1999.